JMEPEG (2010) 19:533–540
DOI: 10.1007/s11665-009-9518-3

1059-9495/$19.00

Microstructure and Tensile Properties of Nanostructured and Ultrafine Grained FeMoB Alloys Produced by Spark Plasma Sintering of Mechanically Alloyed Powders

Cinzia Menapace, Stefano Libardi, Mirco D'Incau, and Alberto Molinari

(Submitted October 29, 2008; in revised form June 9, 2009)

Boron alloyed Fe-1.5%Mo alloys (B from 0.42 to 1.66%) were produced starting from a prealloyed ferrous powder and an elemental boron powder, by mechanical alloying and spark plasma sintering. Near full density samples were obtained (density >99%) with a nano- and ultrafine grained structure, consisting in a ferritic matrix with a fine dispersion of Fe and Mo borides. High boron content and a low sintering temperature are favorable to minimize grain growth on sintering. On increasing the boron content from 0.42% up to 1.66%, yield strength increases and ductility decreases; this effect is enhanced by the sintering temperature because of the structural coarsening. Both ultrafine grained and nanostructured materials have a dimpled ductile fracture. On increasing the crystallite size, a mixed dimpled-cleavage fracture is observed.

Keywords failure analysis, mechanical testing, powder metallurgy

1. Introduction

The structural refining in the submicrometric range causes a large increase in hardness and yield strength and a decrease of the ductile-to-brittle transition temperature of metallic materials, combined with a decrease of tensile ductility due to the occurrence of plastic instability phenomena (Ref 1-4). Among the various methods used to produce nanostructured metals (Ref 5), sintering of high energy milled powders may represent a valid alternative provided that sintering is accomplished by minimal grain growth. The microstructural coarsening can be controlled by second phase particles, stable at the sintering temperature, which provide a drag stress opposing grain boundary mobility [grain boundary pinning (Ref 6)]. The second phase can either be added to the base powder or precipitate during sintering from an oversaturated metallic matrix. In the latter case, alloying elements are introduced during milling (mechanical alloying—MA) to obtain the oversaturated solid solution from which they precipitate on sintering to form the grain boundary pinning compound.

The two approaches have been used to produce a nanostructured iron alloy using spark plasma sintering (SPS) to consolidate an atomized FeMo powder nanostructured by high energy milling. In previous work (Ref 7, 8) SiO_2 and TiO_2 nanoparticles were added to the powder in order to obtain a homogeneous dispersion just after milling, and the structural characteristics as well as the tensile properties have been investigated. In the present work, the approach based on in situ precipitation during consolidation was experimented, adding an elemental boron powder to obtain the oversaturated solid solution by milling. Because of its very low solubility in the ferritic matrix, boron is expected to cause an extensive precipitation of borides on heating during sintering. The interaction between boron and the ferrous matrix has been studied by several authors (Ref 9-14), who used this element to activate free sintering by simply mixing a boron carrier powder to a conventional ferrous powder. MA forms a homogeneous solid solution, and the precipitation on sintering is also expected to be homogeneous and fine. Powder consolidation was done by SPS, since this requires lower temperatures and much shorter times than conventional hot pressing techniques (Ref 15, 16). These characteristics make SPS particularly suitable to the processing of nanostructured powders (Ref 3, 7, 8, 17-21).

Cinzia Menapace, Mirco D'Incau, and **Alberto Molinari**, Department of Materials Engineering and Industrial Technologies, University of Trento, via Mesiano 77, 38050 Trento, Italy; and **Stefano Libardi**, TFM S.p.A., via del Lavoro 34, 36040 Grisignano di Zocco (VI), Italy. Contact e-mail: cinzia.menapace@ing.unitn.it.

2. Experimental Procedure

Mixtures of a pre-alloyed Fe-1.5%Mo powder (Astaloy Mo, Höganäs AB) and an elemental boron powder were prepared in a Turbula mixer. Different amounts of boron were added to obtain the volumetric percentages of Fe_2B reported in Table 1 in the as-sintered microstructure.

In total, 200 g of powder for each alloy composition were ball milled in a Fritsch planetary mono mill "Pulverisette 6" for 15 h, using 250 grinding balls (10 mm diameter) made of 100Cr6. The ball-to-powder weight ratio (BPR) was 5. Milling was carried out in a grinding bowl (500 mL volume) set under static low vacuum (10^{-1} mbar). The rotational speed was 500 rpm and cycles of 9 min on and 33 min off were adopted to avoid overheating.

Table 1 Amounts of boron added to obtain the volumetric percentages of Fe_2B

Target in terms of vol.% Fe_2B	Amount of B, wt.%
5	0.42
10	0.83
15	1.24
20	1.66

The ball milled powder was sieved to determine the particle size distribution and analyzed by x-ray diffraction (XRD) to measure the crystallite size.

The powders were consolidated by SPS in a DR.SINTER® SPS1050 (Sumitomo Coal & Mining, now SPS Syntex Inc.) apparatus with graphite punches and dies. Disks of 30 mm diameter and 5 mm height were produced (six for each material). The SPS parameters are:

- heating under vacuum at 100 °C/min up to the sintering temperature;
- isothermal holding for 1 min;
- a 60 MPa pressure applied at 450 °C; and
- free cooling down to room temperature in the closed die.

Temperature was measured by a K-thermocouple inserted into a blind hole in the die wall according to a procedure adopted in previous studies.

On the sintered specimens, density was measured with the Archimedes method and metallographic investigation was carried out by light optical microscope (LOM) and by scanning electron microscope (SEM) on specimens etched with Nital 2%. By means of XRD, a quantitative analysis of the borides precipitated on sintering was carried out. The Vickers microhardness was measured with a load of 1 N. Tensile tests were carried out on a standard tensile machine (INSTRON 8516). As in other previous works (Ref 8, 22) the specimens for tensile tests were cut by electro discharge machining (EDM) from the disks; shape and dimension of these specimens are shown in Fig. 1. Five samples were machined for each material and then tensile tested.

The fracture surface of the tensile specimens was investigated with the SEM.

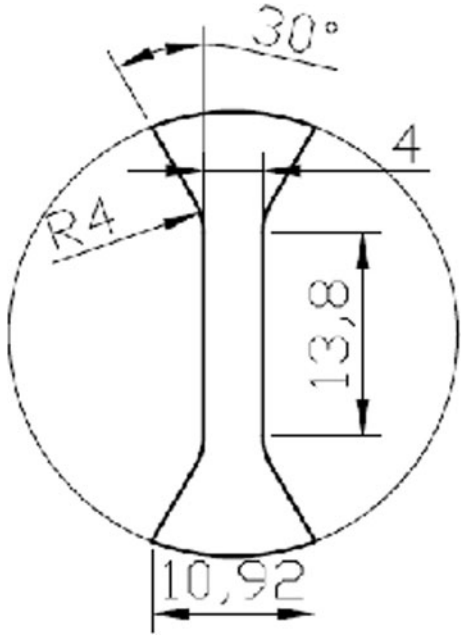

Fig. 1 Specimen for tensile tests cut from the SPSed disks

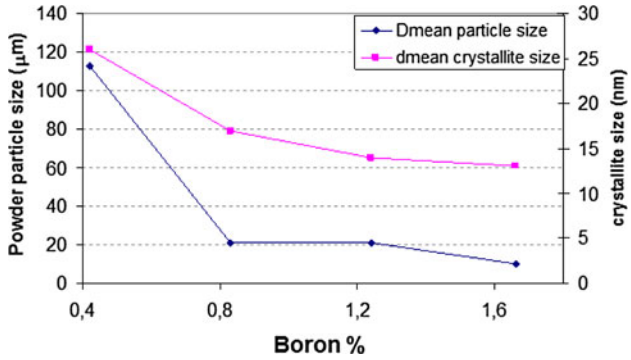

Fig. 2 Mean particle size and mean crystallite size of the milled powder as a function of the boron content

3. Results and Discussion

3.1 Characteristics of the Milled Powders

Figure 2 shows the mean particle size and the mean crystallite size of the milled powders as a function of the boron content.

MA causes a progressive reduction in particle size with increasing boron content; this means that the additive tends to favor the fragmentation of the powder particles against welding, acting as a process control agent (Ref 23). As a consequence, the crystallite size also decreases. All the powders, irrespective of the boron content, are nanostructured. XRD spectra do not reveal any peaks of boron and borides. This result cannot be an indication of the formation of the oversaturated solid solution, because of the intrinsic difficulty of revealing such phases in a nanostructured material. On the other hand, Ref 24 reports the formation of the oversaturated solid solution by MA of a Fe-0.77wt.% B alloy. It may be then assumed that most of the boron added is effectively dissolved in the FeMo lattice.

Because of the small particle size, microhardness was measured only on the B free and 0.42%B powders. Data are shown in Table 2. Since hardening by both grain refining and solid solution is enhanced by boron, it may be reasonably assumed that the other two powders are harder than those reported in the Table 2.

3.2 Spark Plasma Sintering

Powder densification during SPS can be qualitatively monitored by recording the displacement of the lower punch. Figure 3 shows the displacement curve versus temperature and its first derivative (displacement rate), up to 900 °C.

The curves show a step at 450 °C, caused by the application of pressure, followed by a peak at about 700 °C. This peak is due to an acceleration of the densification process, which occurs on heating when the resistance to plastic strain of the

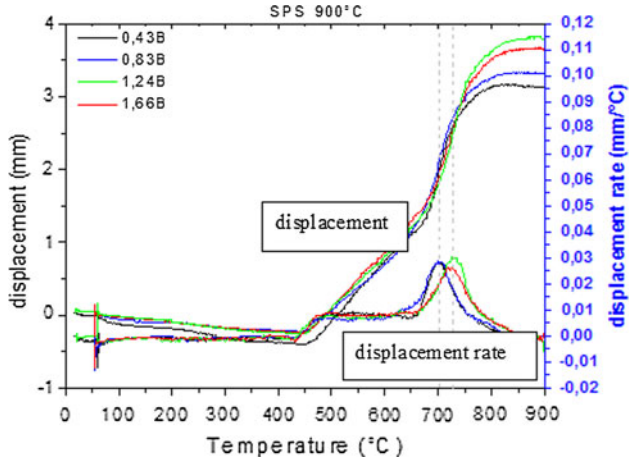

Fig. 3 Displacement and displacement rate of FeMo + B SPSed at 900 °C

Table 2 Microhardness of the MA powders

Powder	HV 0.1
FeMo	692 ± 27
FeMo + 0.42B	700 ± 55

Table 3 Temperature of maximum displacement rate

Powder	Temperature of max displacement rate, °C
FeMo + 0.42B	701
FeMo + 0.83B	701
FeMo + 1.24B	727
FeMo + 1.66B	728

material becomes lower than the effective applied stress (Ref 25), as in conventional hot pressing processes. Under this condition, particles deform plastically and densification rate increases. The temperatures of the peak are reported in Table 3.

The temperatures of the maximum displacement rate of 0.42 and 0.83 wt.% boron powders are lower than those of the other two materials, as might be expected from the different hardness of the powders. In principle, this experimental evidence should be correlated with the resistance to thermal softening (Ref 7) rather than room temperature hardness. As reported below, characterization of the sintered specimens clearly indicates that the resistance to thermal softening increases with the boron content, so the shift to higher temperatures of the densification peak is justified.

Since densification stops at about 850 °C, the specimens for microstructural and mechanical characterization were sintered at 850 and 900 °C.

3.3 Density

Density of the SPSed specimens is reported in Table 4; this is independent of the boron content and the sintering temperature.

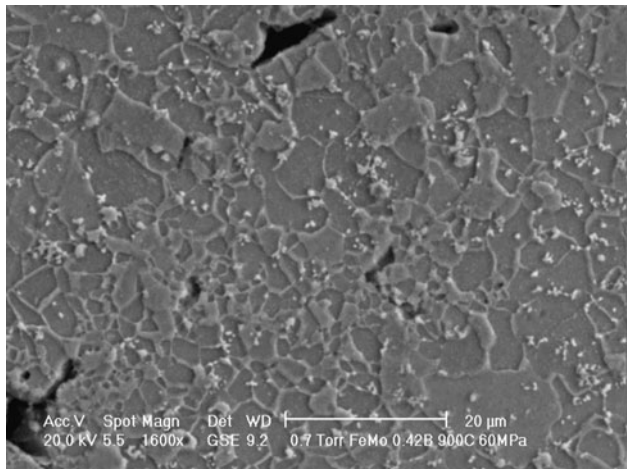

Fig. 4 SEM microstructure of the 0.42wt.%B material SPSed at 900 °C

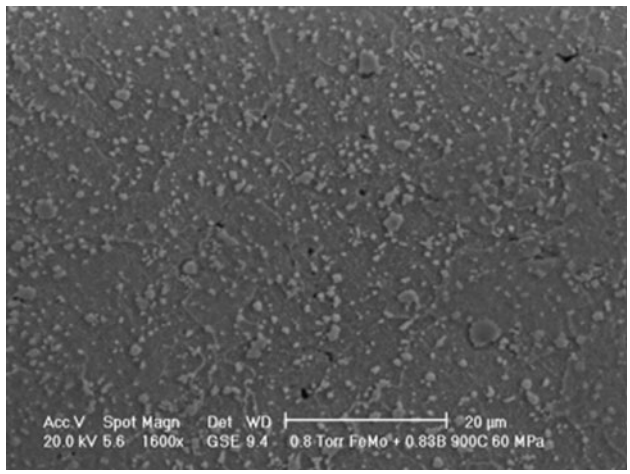

Fig. 5 SEM microstructure of the 0.83wt.%B material SPSed at 900 °C

Table 4 Density of the disks prepared by SPS

Material	ρ, g/cm³	
	T_{SPS} = 850 °C	T_{SPS} = 900 °C
FeMo + 0.42B	7.76	7.73
FeMo + 0.83B	7.74	7.73
FeMo + 1.24B	7.75	7.73
FeMo + 1.66B	7.76	7.74

3.4 Microstructure

At both sintering temperatures, the microstructure of the materials consists in a ferritic matrix with a fine and homogeneous dispersion of borides. As an example, Fig. 4-7 report SEM images of the 900 °C sintered samples. At 850 °C microstructure is finer than at 900 °C.

Some large pores are present in the specimen with the lowest boron content, whilst in the others a homogeneously dispersed microporosity is visible. This difference can be

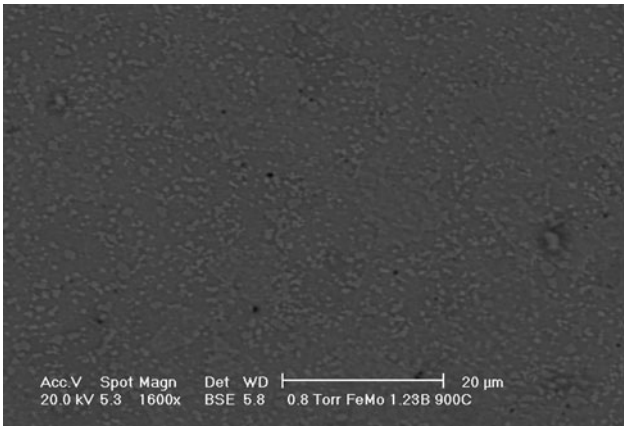

Fig. 6 SEM microstructure of the 1.24wt.%B material SPSed at 900 °C

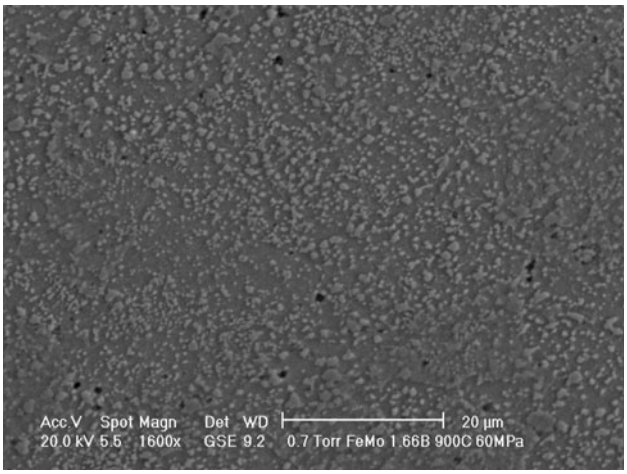

Fig. 7 SEM microstructure of the 1.66wt.%B material SPSed at 900 °C

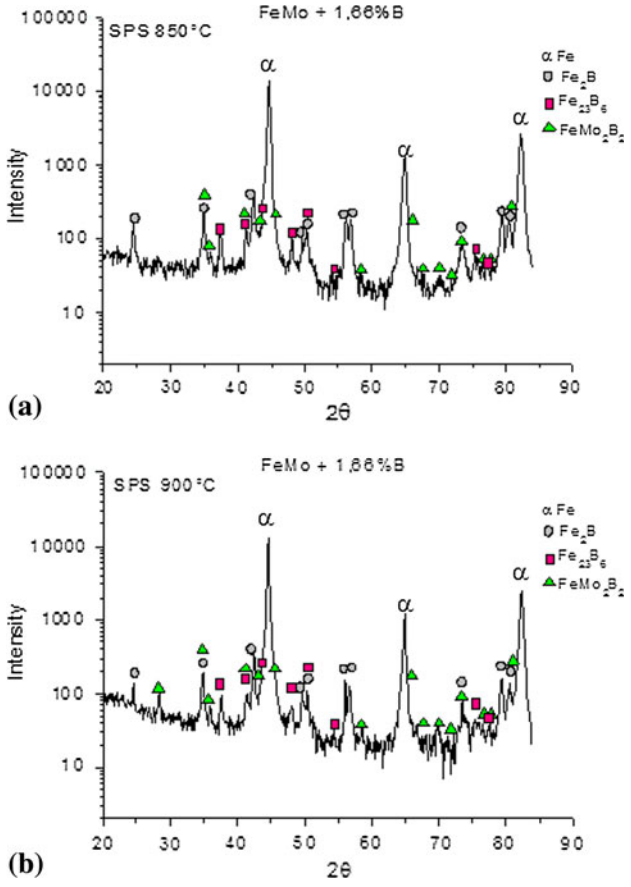

Fig. 8 XRD pattern of 1.66%B sample SPSed at 850 °C (a) and 900 °C (b)

correlated with the particle size, which is much larger in the 0.42% B powder and so is less favorable to a homogeneous densification. Boride particles are very fine and homogeneously distributed in the ferritic matrix. They precipitate during sintering from the oversaturated solid solution, and the homogeneous nucleation is favored by the uniform distribution of boron in the mechanically alloyed powder, as well as by the high density of structural defects which characterize the nanostructure. From this viewpoint, the microstructure is much better than that obtained by free sintering of blended powders, where borides are segregated as a continuous network at the grain boundaries.

The amount of boride particles increases with the boron content.

A quantitative XRD analysis was carried out on all the specimens. Figure 8 shows, as an example, the XRD spectra of the specimens containing 1.66% boron SPSed at the two temperatures.

In addition to ferrite, three types of borides were identified: Fe_2B, $FeMo_2B_2$ and $Fe_{23}B_6$. Whilst the first two borides are stable phases in the Fe-Mo-B system (Ref 11, 26, 27), the third one is a metastable phase, which has been obtained in a

Table 5 Borides volume percentage measured by XRD

Material	SPS temperature 850 °C	SPS temperature 900 °C
FeMo + 0.42B	6	5.9
FeMo + 0.83B	11.1	11.8
FeMo + 1.24B	15.8	15.6
FeMo + 1.66B	20.2	21.5

macroscopic amount only by mechanical alloying (Ref 28). It can be stabilized by the substitution of Fe atoms by another transition metal atom, and has been observed as a product of secondary crystallization of amorphous ribbons (Ref 29). The slight discrepancy between the lattice parameters reported in Ref 30 and those measured by XRD in the present study supports the hypothesis that some Mo replaces Fe atoms, stabilizing the ternary compound $(Fe,Mo)_{23}B_6$. The total amount of borides is reported in Table 5, and corresponds quite well to that hypothesized on designing the composition of the alloy (Table 1), even though it comprises the three types of compound and not only Fe_2B. The volumetric percentage of borides does not depend on temperature, indicating that precipitation is completed during the heating step.

The different kinds of borides are visible in the SEM micrograph of Fig. 9 (5000×), which refers to material FeMo + 1.66%B sintered at 850 °C. Borides show different

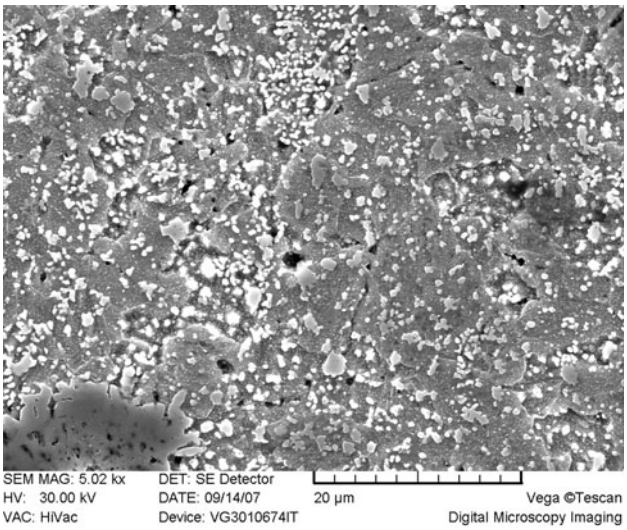

Fig. 9 SEM micrograph of the 1.66wt.%B material SPSed at 850 °C

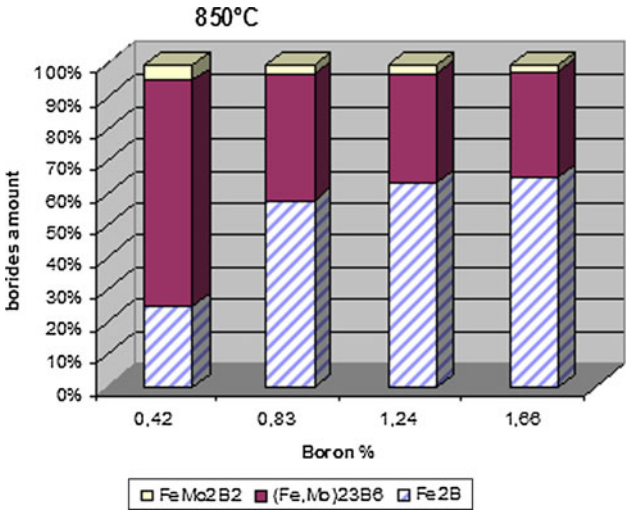

Fig. 10 Percents of the three borides in samples SPSed at 850 °C

morphologies: some are bigger and irregular, other are smaller and rounder.

The relative amounts of the three types of boride are reported in Fig. 10 and 11. The increase in the boron content results in a progressive increase in the relative percentage of Fe_2B, with a corresponding decrease of the other two borides. Moreover, for each boron content, $FeMo_2B_2$ and Fe_2B increase with the SPS temperature, while $(Fe,Mo)_{23}B_6$ decreases because of its metastability.

The precipitation of borides changes the theoretical density of the four materials. Density of the borides is 7.30 g/cm^3 (Fe_2B) and 8.44 g/cm^3 ($FeMo_2B_2$) whilst for $(Fe,Mo)_{23}B_6$ it is not available; it is 7.38 g/cm^3 for $Fe_{23}B_6$ and is expected to increase due to the presence of substitutional Mo. Assuming the same Fe/Mo ratio of the base powder, density of the metastable boride is 7.43 g/cm^3. Theoretical density of the various sintered materials was then calculated using data from Fig. 9 and 10 and used to evaluate densification attained by SPS at the two

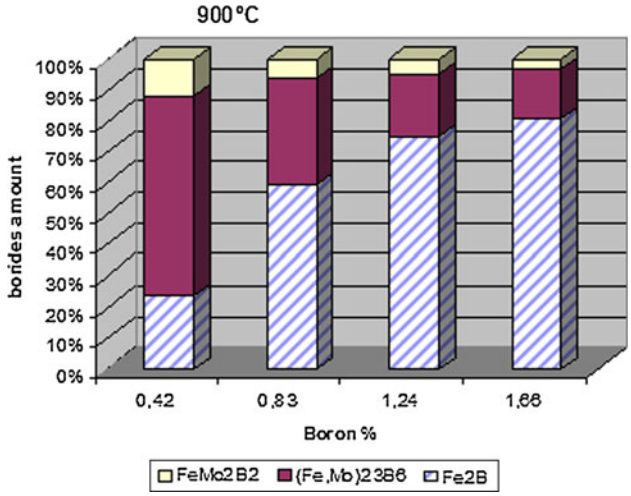

Fig. 11 Percents of the three borides in samples SPSed at 900 °C

Table 6 Relative densification of the sintered specimens

Material	SPS temperature 850 °C	SPS temperature 900 °C
FeMo + 0.42B	99.3	98.8
FeMo + 0.83B	99.3	99.2
FeMo + 1.24B	99.8	99.5
FeMo + 1.66B	100	100

Table 7 Microhardness of the SPSed specimens

	HV 0.1	
Material	850 °C	900 °C
FeMo + 0.42B	228 ± 9	187 ± 4
FeMo + 0.83B	302 ± 14	200 ± 9
FeMo + 1.24B	355 ± 7	234 ± 4
FeMo + 1.66B	384 ± 7	256 ± 6

temperatures. Results are shown in Table 6, indicating that densification tends to increase with the boron content.

3.5 Microhardness and Tensile Properties

Microhardness of the various materials is reported in Table 7. It increases with the boron content and decreases with the sintering temperature.

Microhardness depends on grain size and on the amount of borides.

The crystallite size of ferrite can be precisely determined by the half-height width of XRD peaks in the nanometric range, up to 150-200 nm. Over this range, the peak width is not significant of the crystallite size. The elaboration of XRD spectra shows that only the 1.66%B material sintered at 850 °C is still in the nanometric range, the crystallite size being around 150 nm. In the other cases, crystallite size is larger and cannot be determined by the peak width. The SEM investigation reveals a grain size of a few micrometers in the materials containing the lowest amount of boron, whilst in the others the homogeneous dispersion of borides does not allow the grain

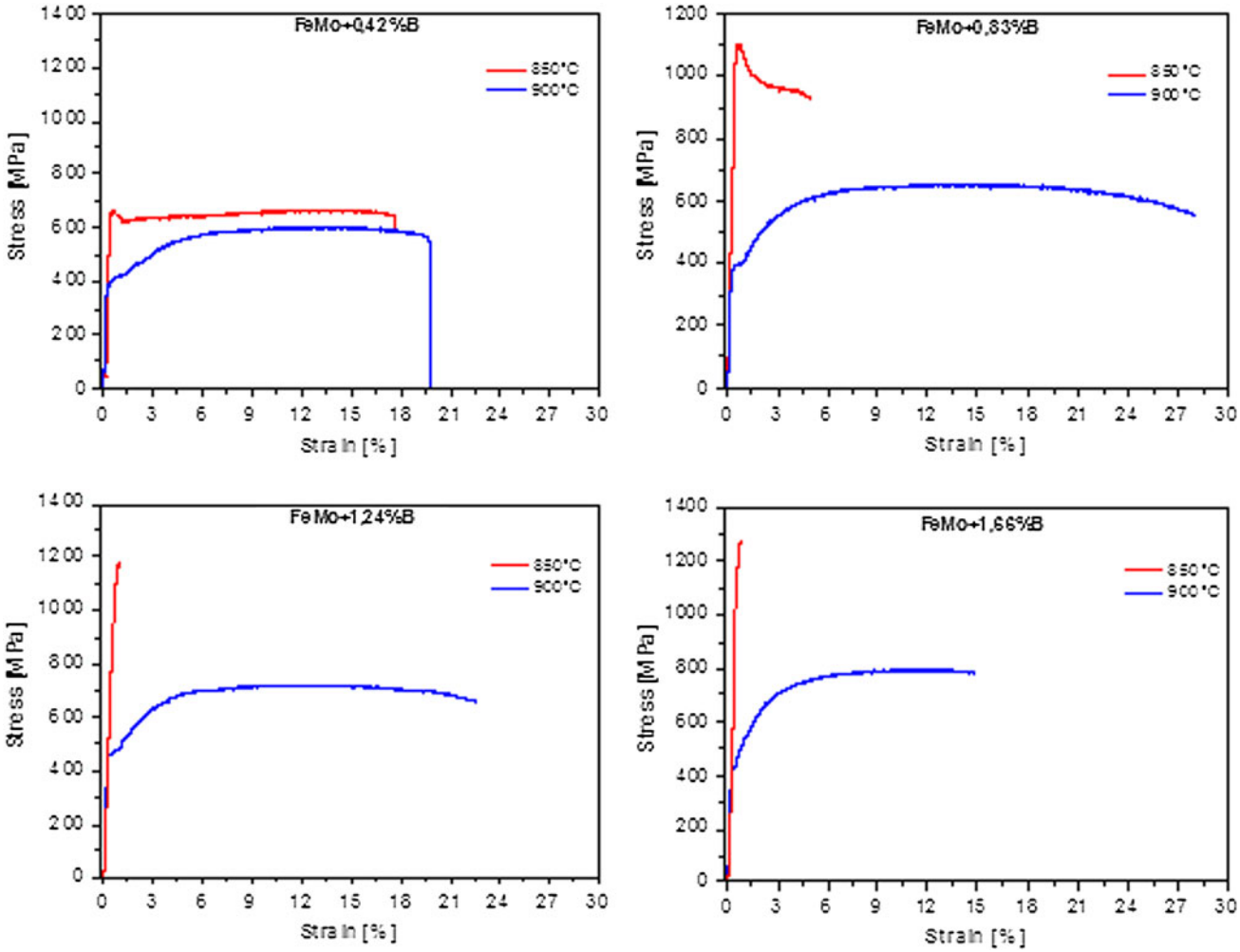

Fig. 12 Tensile curves of the materials investigated

boundary to be revealed by metallographic etching. Since the precipitation of borides is expected to oppose grain growth by grain boundary pinning, it might be assumed that the crystallite size increases with decreasing boron content, as well as with increasing temperature, over the entire range from 150 nm to 5 μm.

The contribution of borides to microhardness is obvious, being harder than the ferritic matrix; the increase in their volumetric percent results in a microstructural hardening.

The effect of SPS temperature cannot be attributed to borides, since their amount does not change; it simply depends on the structural coarsening.

Figure 12 shows an example of the stress-strain tensile curves of all the materials. They were chosen, among the five tested samples, since they are representative of the material tensile behavior.

The curves show an evident difference between the materials sintered at 850 °C and those sintered at 900 °C. While the specimens sintered at the highest temperature (900 °C) show a sharp yield point followed by strain hardening and uniform deformation, those sintered at 850 °C show a different behavior. In particular:

– a sharp yield point followed by uniform deformation with poor strain hardening for the material with 0.42%B;
– only non-uniform deformation for the 0.83%B material; and
– no plastic strain for the two other materials (1.24% and 1.66%B).

With the exception of the material with the lowest boron content, the behavior of the materials sintered at 850 °C is typical of ultrafine grained and nanostructured materials. The increase in the flow stress over the strain hardening rate determines the conditions of plastic instability, which results in the lack of work hardening during plastic deformation (Ref 1). On decreasing the crystallite size, a transition from conventional plastic behavior (0.42%B) to non-uniform plasticity (0.83%B) and further to brittle behavior (1.24%B and 1.66%B) is induced.

Tensile properties are reported in Table 8.

The best tensile strength is attained on sintering at 850 °C. The structural refining results in a high yield stress at the expenses of ductility. The properties of the materials containing 0.83%B and 1.66%B are interesting in terms of strength-ductility combination (0.83%B) and strength (1.66%B). Both the materials show a dimpled fracture surface, as shown by Fig. 13 and 14. A similar ductile fracture surface was seen in 0.42%B materials too, with a mean grain size of some microns. The only difference observed between these fracture surfaces is

Table 8 Tensile properties of the SPSed materials

Material	SPS temperature 850 °C			SPS temperature 900 °C		
	σy, MPa	UTS, MPa	Elongation, %	σy, MPa	UTS, MPa	Elongation, %
FeMo + 0.42B	662 ± 4	669 ± 8	17.7 ± 1.7	386 ± 5	598 ± 7	19.8 ± 1.2
FeMo + 0.83B	1103 ± 13	1103 ± 13	5 ± 0.9	390 ± 5	656 ± 5	28 ± 2.2
FeMo + 1.24B	1176 ± 11	1176 ± 11	1 ± 0.2	451 ± 8	724 ± 11	22.6 ± 2.5
FeMo + 1.66B	1280 ± 16	1280 ± 16	0.9 ± 0.1	426 ± 4	796 ± 9	14.8 ± 1.7

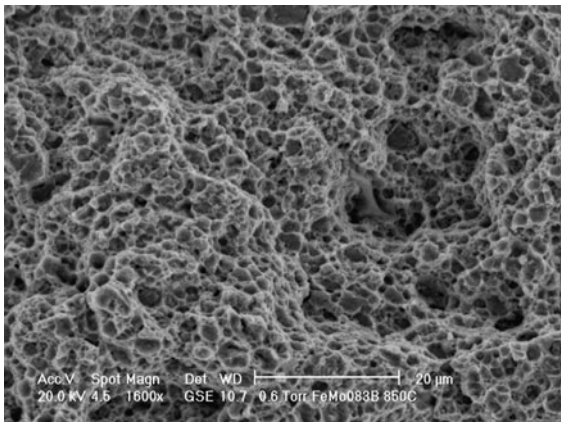

Fig. 13 Fracture surface of 0.83%B material SPSed at 850 °C

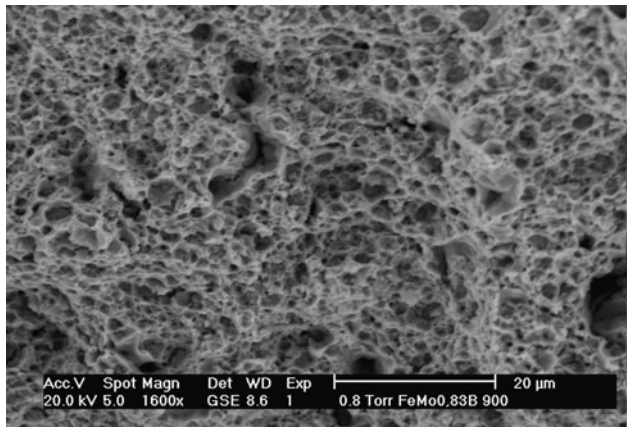

Fig. 15 Fracture surface of 0.83%B material SPSed at 900 °C

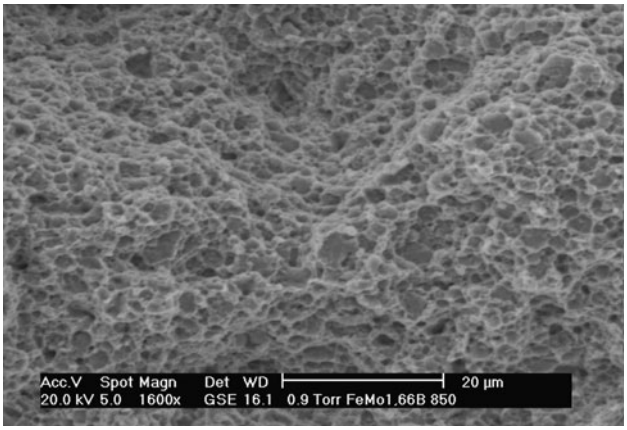

Fig. 14 Fracture surface of 1.66%B material SPSed at 850 °C

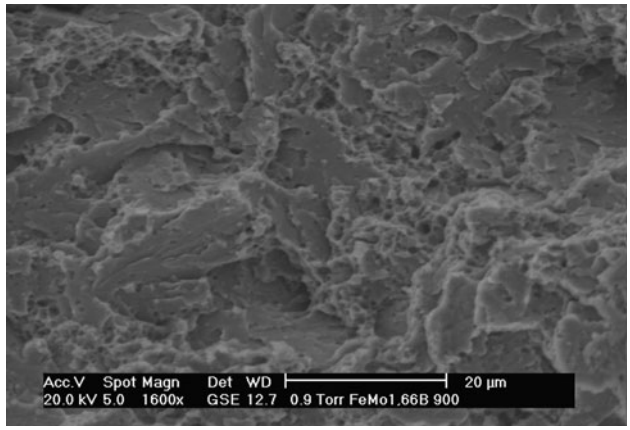

Fig. 16 Fracture surface of 1.66%B material SPSed at 900 °C

the depth of dimples, which appear much more strained in 0.42%B and 0.83%B than in 1.66%B as a consequence of the much higher plastic deformation. The dimpled fracture surface is typically observed in conventional polycrystalline materials as well as in both ultrafine grained and nanocrystalline materials with dimples size of the same order of magnitude (Ref 4). Some of these fracture surfaces were defined as "transgranular ductile" in experiments carried out on nanocrystalline nickel (Ref 31, 32) where a transgranular-tearing fracture mode was observed. In the present study, this is observed in the alloys containing more than 0.42%B sintered at 850 °C that are ultrafine grained.

Sintering at 900 °C promotes structural coarsening to such an extent that strength drops with respect to the corresponding materials treated at 850 °C. The rise of ductility is also a consequence of the structural coarsening. The fracture surface of the materials containing 0.83%B and 1.66%B is shown in Fig. 15 and 16, for comparison with the two previous ones.

The fracture morphology is ductile in the 0.83%B material and mixed (dimpled-cleavage) in the other. The comparison between the 1.66%B materials sintered at the two temperatures is interesting showing the effect of the nanostructure in opposing propagation of the cleavage cracks. Despite the

higher microhardness, fracture is dimpled in the material sintered at 850 °C, whilst many cleavages appear in the other.

4. Conclusions

A pre-alloyed 1.5wt.%Mo ferrous powder was mechanically alloyed with differing amounts of elemental boron (from 0.42 to 1.66 wt.%) to produce an oversaturated nanostructured solid solution. The MA powders were then consolidated by SPS at 850 and 900 °C. On heating to the sintering temperature, a very fine and homogeneous precipitation of boride particles occurs, which counteracts grain growth. Sintered materials have density very close to the theoretical and crystallite size ranging between 150 nm and a few micrometers, depending on the boron content and the SPS temperature. The tensile properties depend on the microstructure. Significant strengthening was obtained on sintering at 850 °C, thanks to the ultrafine grained structure. On increasing the boron content from 0.42 to 1.66%, the yield strength increases and ductility decreases, due to progressive lack of work hardenability. Tensile strength around 1100 MPa was obtained with 5% elongation at fracture in the 0.83%B alloyed material. On increasing the boron content, strength further increases to 1300 MPa, with a corresponding decrease of elongation at fracture down to 1%. Both ultrafine grained and nanostructured materials have a dimpled ductile fracture. On increasing the crystallite size, a mixed dimpled-cleavage fracture is observed, confirming the positive effect of the crystallite size on the resistance to propagation of the brittle fracture.

References

1. S. Takaki, K. Kawasaki, and Y. Kimura, Mechanical Properties of Ultra Fine Grained Steels, *J. Mater. Process. Technol*., 2001, **117**, p 359–363
2. N. Tsuji, Y. Ito, Y. Saito, and Y. Minamino, Strength and Ductility of Ultrafine Grained Aluminum and Iron Produced by ARB and Annealing, *Scr. Mater.*, 2002, **47**, p 893–899
3. D.P. Harvey, R. Kalyanaraman, and T.S. Sudarshan, Consolidation and Mechanical Behaviour of Nano-Crystalline Iron Powder, *Mater. Sci. Technol.*, 2002, **18**, p 959–963
4. M.A. Meyers, A. Mishra, and D.J. Benson, Mechanical Properties of Nanocrystalline Materials, *Prog. Mater. Sci.*, 2006, **51**, p 427–556
5. R. Song, D. Ponge, D. Raabe, J.G. Speer, and D.K. Matlock, Overview of Processing, Microstructure and Mechanical Properties of Ultrafine Grained bcc Steels, *Mater. Sci. Eng. A*, 2006, **441**, p 1–17
6. R.E. Reed-Hill, *Physical Metallurgy Principles*, PWS-KENT Publishing Company, Boston, MA, 1973, p 262–267
7. S. Libardi, M. Leoni, L. Facchini, M. d'Incau, P. Scardi, and A. Molinari, Effect of the Dispersion of Nanometric Silica Particles on the Thermal Stability of a Nanostructured Iron Based Powder, *Mater. Sci. Eng. A*, 2007, **445**, p 244–250
8. S. Libardi, M. Zadra, F. Casari, and A. Molinari, Mechanical Properties of Nanostructured and Ultrafine-Grained Iron Alloys Produced by Spark Plasma Sintering of Ball Milled Powders, *Mater. Sci. Eng. A*, 2008, **478**, p 243–250
9. M. Sarasola, T. Gomez-Acebo, and F. Castro, Liquid Generation During Sintering of Fe-3.5%Mo Powder Compacts with Elemental Boron Additions, *Acta Mater.*, 2004, **52**, p 4615–4622
10. A. Molinari, T. Pieczonka, J. Kazior, S. Gialanella, and G. Straffelini, Dilatometry Study of the Sintering Behaviour of Boron Alloyed Fe-1.5%Mo Powder, *Metall. Mater. Trans. A*, 2000, **3**, p 1497–1506
11. R.M. German, K.S. Hwang, and D.S. Madan, Analysis of the Fe-Mo-B Sintered Alloys, *Powder Metall. Int.*, 1987, **19**(2), p 15–18
12. E. Dudrova, M. Selecka, R. Bures, and M. Kabatova, Effect of Boron Addition on Microstructure and Properties of Sintered Fe-1.5Mo Powder Materials, *ISIJ Int.*, 1997, **1**, p 59–64
13. J. Liu, R.M. German, A. Cardamone, T. Potter, and F.J. Semel, Boron-Enhanced Sintering of Iron-Molybdenum Steels, *Int. J. Powder Metall.*, 2001, **37**(5), p 39–46
14. T. Ide, K. Nakano, and T. Ando, Effects of Mo Content and Sintering Temperature on the Strength, Hardness and Density of Fe-6 mass%B – x mass% Mo Alloys, *Powder Metall. Int.*, 1988, **20**(3), p 21–24
15. M. Tokita, *Proceedings of 2000 Powder Metallurgy World Congress*, Part 1, K. Kosuge and H. Nagai, Ed., November 2000 (Kyoto, Tokyo, Japan), The Japan Society of Powder and Powder Metallurgy, 2000, p 729–732
16. H.W. Zhang, R. Gopalan, T. Mukai, and K. Hono, Fabrication of Bulk Nanocrystalline Fe–C Alloy by Spark Plasma Sintering of Mechanically Milled Powder, *Scr. Mater.*, 2005, **53**(7), p 863–868
17. M. Kawahara et al., *Proceedings of 2000 Powder Metallurgy World Congress*, Part 1, K. Kosuge and H. Nagai, Ed., November 2000 (Kyoto, Tokyo, Japan), The Japan Society of Powder and Powder Metallurgy, 2000, p 741–745
18. T. Yamamoto, H. Kitaura, Y. Kodera, T. Ishii, M. Ohyanagi, and Z.A. Munir, Consolidation of Nanostructured Beta-SiC by Spark Plasma Sintering, *J. Am. Ceram. Soc.*, 2004, **87**(8), p 1436–1441
19. R. Chaim, Densification Mechanisms in Spark Plasma Sintering of Nanocrystalline Ceramics, *Mater. Sci. Eng. A*, 2007, **443**, p 25–32
20. M. Zadra, F. Casari, and A. Molinari, Microstructure and Mechanical Properties of Nanostructured Aluminium Consolidated by SPS, *Mater. Sci. Forum*, 2007, **534–536**, p 1401–1404
21. L. Girardini, M. Zadra, F. Casari, and A. Molinari, Bulk Fine Grained and Nanostructured Binderless WC Consolidation by Spark Plasma Sintering, *Proceedings EURO PM2007*, Vol 3 (Toulouse), 15–17 October 2007, EPMA, Shrewsbury, UK, p 77–82
22. M. Zadra, F. Casari, L. Girardini, and A. Molinari, Spark Plasma Sintering of Pure Aluminium Powder: Mechanical Properties and Fracture Analysis, *Powder Metall.*, 2007, **50**(1), p 40–45
23. C. Suryanarayana, Mechanical Alloying and Milling, *Prog. Mater. Sci.*, 2001, **46**, p 1–184
24. R.J. Perez, B.L. Huang, P.J. Crawford, A.A. Sharif, and E.J. Lavernia, Synthesis of Nanocrystalline Fe-B-Si Powders, *Nanostruct. Mater.*, 1996, **7**, p 47–56
25. H.V. Atkinson and S. Davies, Fundamental Aspects of Hot Isostatic Pressing: An Overview, *Metall. Mater. Trans. A*, 2000, **31**, p 2981–3000
26. T. Ide and T. Ando, Reaction Sintering of an Fe-6wt.%B-48wt%Mo Alloy in the Presence of Liquid Phase, *Metall. Trans. A*, 1989, **20**, p 17–24
27. K. Takagi, T. Watanabe, T. Ando, and Y. Kondo, Effect of Molybdenum and Carbon properties of Iron Molybdenum Boride Hard Alloys, *Int. J. Powder Metall.*, 1986, **22**(2), p 91–96
28. V.A. Barinov, V.A. Tsurin, and V.I. Voronin, Mössbauer Investigations of the Metastable $Fe_{23}B_6$ Phase, *Phys. Met. Metallogr.*, 2006, **101**(5), p 456–466
29. J. Long, P.R. Ohodnicki, D.E. Laughlin, and M.E. McHenry, Structural Studies of Secondary Crystallization Products of the Fe23B6-Type in a Nanocrystalline FeCoB-Based Alloy, *J. Appl. Phys*., 2007, **101**, p 09N114-1-3
30. Y. Kahn and H. Wibbeke, Formation of the τ-Phase in the Fe-B Alloys, *Z. Metallkd.*, 1991, **82**(9), p 703–705
31. C. Xiao, R.A. Mishrams, S.H. Wang, and W.M. Yin, Tensile Behaviour and Fracture in Nickel and Carbon Doped Nanocrystalline Nickel, *Mater. Sci. Eng. A*, 2001, **301**, p 35–43
32. R.A. Mishrams, C. Xiao, S.H. Wang, and W.M. Yin, R-Curve Characterization of the Fracture Toughness of Nanocrystalline Nickel Thin Sheets, *Mater. Sci. Eng. A*, 2001, **315**, p 21–27